Photogrammetrie • Fernerkundung • Geoinformation 5/2009, S. 407 – 419

Interferometric Potential of High Resolution Spaceborne SAR

Richard Bamler, Michael Eineder, Nico Adam, Xiaoxiang Zhu & Stefan Gernhardt, München & Oberpfaffenhofen

Keywords: Synthetic Aperture Radar (SAR), SAR interferometry, Spotlight SAR, TerraSAR-X, SAR Tomography, Persistent Scatterer Interferometry

Summary: The new class of high resolution spaceborne SAR systems, like TerraSAR-X and COSMO-Skymed opens new possibilities for SAR interferometry. The 1m resolution is particularly helpful when 2D, 2.5D, 3D, or 4D (space-time) imaging of buildings and urban infrastructure is required, where the non-interferometric interpretation of SAR imagery is difficult. Structure and deformation of individual buildings can be mapped, rather than only coarse deformation patterns of areas. The paper demonstrates several new developments in high resolution SAR interferometry using TerraSAR-X as an example. Of particular interest is the very high resolution spotlight mode, which requires some care in interferometric processing. Results from interferometry, Persistent Scatterer Interferometry (PSI), and tomographic SAR in urban environment are presented. The high resolution of TerraSAR-X also supports accurate speckle and feature tracking. An example of glacier monitoring is shown and discussed.

Zusammenfassung: *Neue Möglichkeiten der SAR-Interferometrie durch hochauflösende Weltraum gestützte SAR-Systeme.* Die neue Generation hochauflösender SAR-Satelliten, wie TerraSAR-X und COSMO-Skymed, eröffnen neue Möglichkeiten in der SAR-Interferometrie. Die Auflösung von ca. 1m wird vor allem benötigt, wenn Gebäude und urbane Infrastruktur 2-, 2,5-, 3- oder 4-dimensional abgebildet werden sollen. Gerade diese Objekte sind in nicht-interferometrischen SAR-Bildern schlecht zu interpretieren. So können nun Struktur und Deformation einzelner Gebäude interferometrisch aus dem Weltraum vermessen werden, wo bisher nur grobe Deformationsmuster einer Stadt erfassbar waren. In diesem Aufsatz werden mehrere neue Entwicklungen der hochauflösenden SAR-Interferometrie am Beispiel TerraSAR-X vorgestellt. Von besonderem Interesse sind dabei Daten aus dem Spotlight-Modus, deren interferometrische Verarbeitung erläutert wird. Ergebnisse aus Interferometrie, Persistent Scatterer Interferometrie (PSI) und SAR-Tomographie werden präsentiert. Die Anwendung von Speckle Tracking und Feature Tracking zur Erfassung von Gletscherbewegungen wird demonstriert.

1 Introduction

In 2007 Synthetic Aperture Radar (SAR) remote sensing from space (Bamler & Hartl 1998) made a big leap forward. With the German TerraSAR-X and the Italian COSMO-Skymed satellites have been launched that deliver SAR data with a spatial resolution of up to 1 m compared to typically 10 – 25 m available so far. The advantage of very high resolution (VHR) imagery for cartographic applications is obvious. The real potential of this class of SAR data, however, lies in applications, where the coherent nature of SAR data is exploited, like interferometry or tomography. The 1m resolution is particularly helpful when it comes to 2D, 2.5D, 3D, or 4D imaging of buildings and urban structures. The inherent spatial scales of buildings are dominated by the typical height between floors of 3 – 4 m. Hence, for imaging of urban structures we can expect a tremendous improve-

DOI: 10.1127/1432-8364/2009/0029 1432-8364/09/0029 $ 3.25

ment in information content with the new VHR data.

This paper presents recent results of TerraSAR-X interferometric data exploitation. The results are representative for the potential of all of the new VHR SAR systems.

2 TerraSAR-X Data Characteristics

TerraSAR-X can be operated in three basic resolution modes (cf. Fig. 1; Buckreuss 2003):

- *Stripmap* is the standard mode. It allows imaging of long strips at a ground resolution of about 3 m. The swath width is about 40 km.
- *Spotlight* mode uses electronic antenna beam sweeping to increase the coherent integration time, and, hence, the resolution. The beam steering range is ±0.75°. Up to 249 different azimuth patterns are sequentially activated to approximate a continuous beam sweep. 1m resolution in azimuth can be achieved. Depending on the transmitted bandwidth slant range resolutions are 1.2 m (@ 150 MHz signal bandwidth) or 0.6 m (@ 300 MHz). The downside is that in spotlight mode only short scene lengths and narrow swaths of 5 – 10 km can be acquired, which are, however, sufficient for most investigations in urban environments.
- *ScanSAR* is a mode of an increased swath width of 100 km at the expense of resolution (ScanSAR product resolution: 17 m).

These resolution modes are available at different look angles (20° – 55°) and different polarizations, which makes TerraSAR-X an extremely flexible SAR instument.

An important advantage of TerraSAR-X compared to competitors is the high absolute geometric accuracy of the final data products. Every pixel is absolutely georeferenced to within 0.5 – 1 m, provided that an accurate digital surface model is available. This has been achieved by a precise orbit determination and a careful calibration of all instrumental and physical timing error sources, e. g., tropospheric signal delay. Another advantage of TerraSAR-X is its short revisit time of 11 days. It allows generating interferometric data stacks three times as fast as with ENVISAT/ASAR with its 35 days revisit cycle.

For interferometric applications the short X-band wavelength of 3.1 cm is not optimum, since many objects that remain coherent at longer wavelengths will decorrelate rapidly. Even low vegetation is subject to strong temporal decorrelation at this wavelength. On the other hand, the short wavelength lets surfaces appear rough that would be smooth at longer wavelengths. E. g., roads or flat roofs, which show up as totally black in longer wavelength images, have proven to give sufficient backscatter with TerraSAR-X to be exploited as interferometrically useful objects.

3 Spotlight Interferometry

The focused complex TerraSAR-X spotlight images are represented in zero-Doppler coordinates. Due to the quais-continuous beam steering during data acquisition, however, there is a systematic Doppler centroid drift in

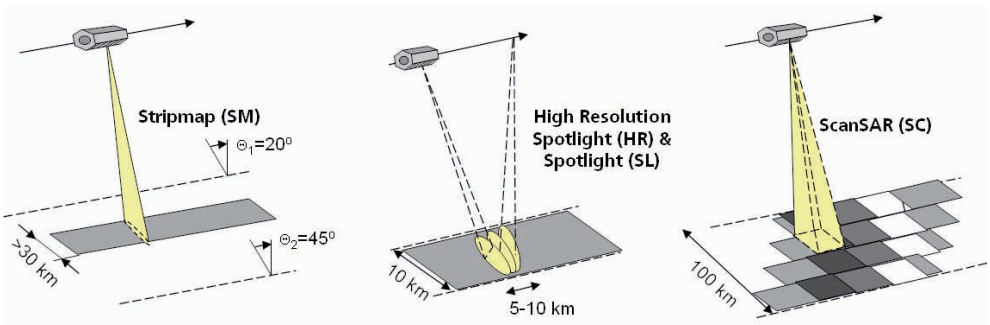

Fig. 1: Basic imaging modes of TerraSAR-X (Buckreuss 2003).

azimuth direction which must be accounted for during all subsequent InSAR processing steps (Eineder et al. 2009). Fig. 2 shows the variation of the processed azimuth spectrum of a typical TerraSAR-X product. Although the sampling rate is sufficient to avoid aliasing, the linear drift and the wraps to the principal sampling band are significant. In consequence, the center frequency of the interpolation kernels, used for interferometric image coregistration, must be adjusted in azimuth (band-pass interpolator of varying center frequency). Also the azimuth common band spectral filtering needs to be updated accordingly. These required operations complicate processing so that standard interferometric processing systems can not be used. We have integrated spotlight capabilities into DLR's InSAR processing software GENESIS early enough to be ready for launch of TerraSAR-X. Therefore, we were able to process spotlight interferograms already during the commissioning pha-

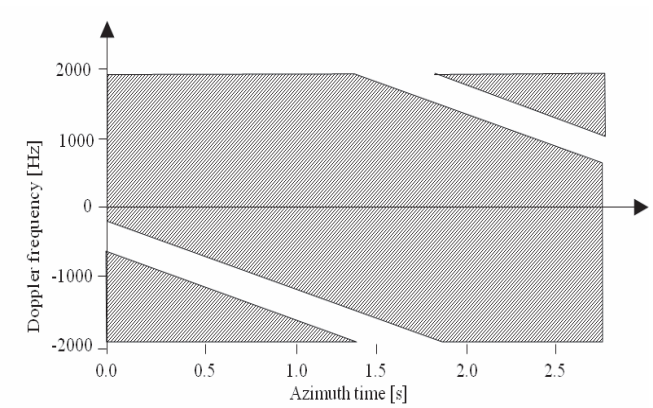

Fig. 2: Support (grey) of time-varying Doppler spectrum of a complex TerraSAR-X spotlight image.

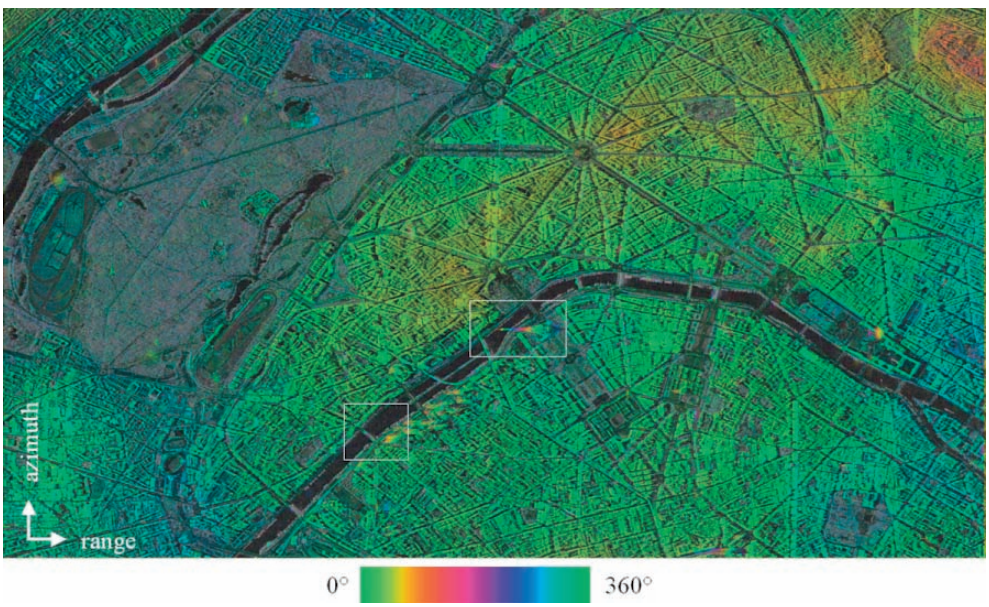

Fig. 3: Flat earth phase corrected TerraSAR-X spotlight interferogram (city of Paris).

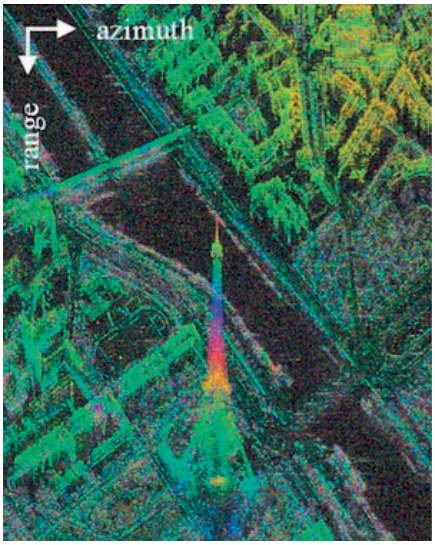

Fig. 4: Zoom of Fig. 3: TerraSAR-X spotlight interferogram of the Eiffel tower. One phase cycle corresponds to 321 m height.

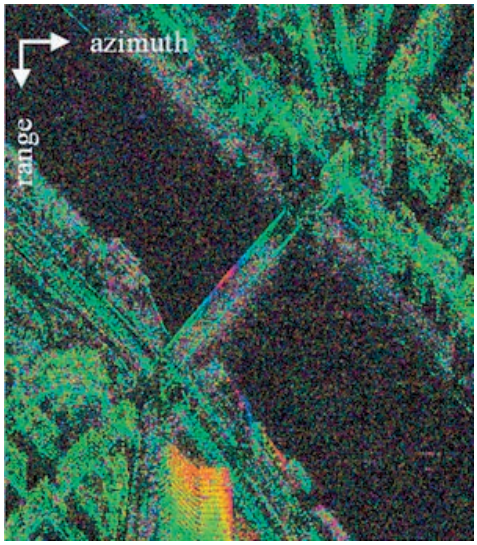

Fig. 5: Zoom of Fig. 3: TerraSAR-X spotlight interferogram of the Mirabeau bridge in Paris. It shows phase changes of 270°. This can be interpreted as a bump of 240 m or (realistically) as a deformation between acquisitions of 12 mm in the radar line of sight direction.

se (Adam et al. 2007). The interferogram of the city of Paris (cf. Fig. 3) and the detail views shown in Figs. 4 and 5 demonstrate the wealth of information in this new class of data.

4 Persistent Scatterer Interferometry (PSI)

Persistent Scatterer Interferometry (PSI) has been introduced in 1999 (Ferretti et al. 2001) as a methodology for long-term monitoring of subsidence, preferably in urban environment. Typically 20 – 100 interferometric data sets of the same area taken from repeat orbit cycles are stacked for PSI analysis. Each pixel in each interferogram is characterized by its range and azimuth coordinates as well as by the temporal and the spatial baselines of the interferogram it belongs to. These four coordinates allow for a much better data analysis than possible from a single interferogram, where temporal and spatial baselines are fixed. The goal of the PSI analysis is to separate the following contributions to the interferometric phase:

- *Elevation of the point:* Elevation is the spatial coordinate orthogonal to range and azimuth. Its phase contribution is proportional to the spatial baseline.
- *Deformation rate:* If linear deformation, e. g., subsidence, can be assumed, its phase contribution is proportional to the temporal baseline. If the deformation is non-linear often some other parameterized temporal model is assumed whose parameters are adjusted.
- *Orbit errors and tropospheric water vapor delay:* These are spatially long wavelength patterns and and temporally uncorrelated.

By exploiting these proportionalities and correlation properties, elevation and deformation rate can be estimated. Fig. 6 shows the PS location in 3D on Hotel Bellagio in Las Vegas and provides an example for the DEM update and Fig. 7 illustrates an example (Las Vegas Convention Center) for the deformation estimation.

Since the data stacks cover a time span of months or years, i. e., much longer than the coherence times of distributed objects (e. g.,

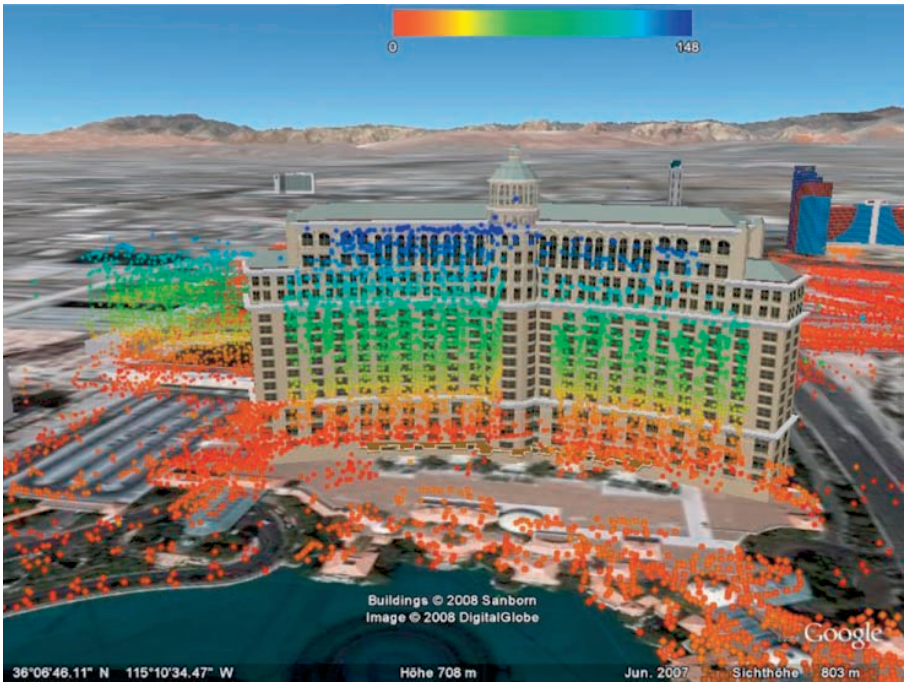

Fig. 6: The color coded elevation estimated by the PSI processing facilitates a geocoding of the PSs [unit: m]. This example presents the 3D location precision and the PS density which perfectly provides the shape of the building's front (Hotel Bellagio, Las Vegas). Note that the Google-Earth building model is too broad.

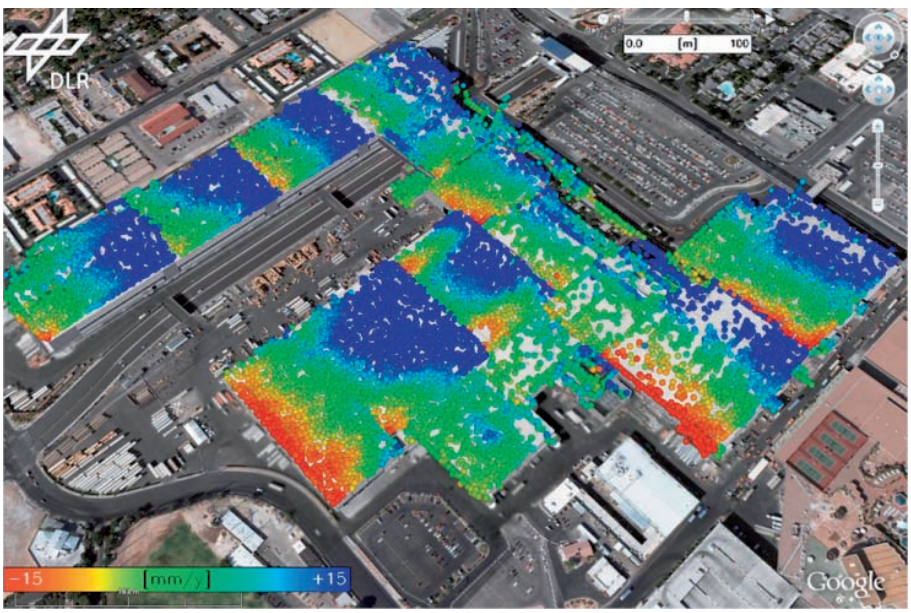

Fig. 7: The PS density of TerraSAR-X allows monitoring the structural stress of buildings. This example presents the deformation (red to blue: –15 mm/y to +15 mm/y) which results from thermal delation of the building's roof (Las Vegas Convention Center).

vegetation), PSI performs all the analysis steps only on bright temporarily stable points, the so-called persistent, or permanent, scatterers (PSs). They are identified in the data stacks by metrics like signal-to-clutter-ratio. In pactise, the SCR allows an ensemble estimate and a prediction of the phase stability. Typical PSs are metallic structures (gratings, poles), facade or roof elements that act as dihedral or trihedral corner reflectors, etc.

PSI has been applied very successfully with medium resolution SAR data from ERS-1/2 and ENVISAT/ASAR. Subsidence rate accuracies of better than 1 mm/a have been reported (Ferretti et al. 2007; Adam et al. 2009) However, the physical interpretation of these estimates has proven difficult. The low resolution does not give access to details of the buildings. The PSs appear to be quite randomly distributed at a density of about 100–500 PS/km^2, i. e., one PS per block of 100 m × 100 m to 50 m × 50 m. There is no guarantee that a particular building of interest is represented by a PS. It is also difficult to differentiate between

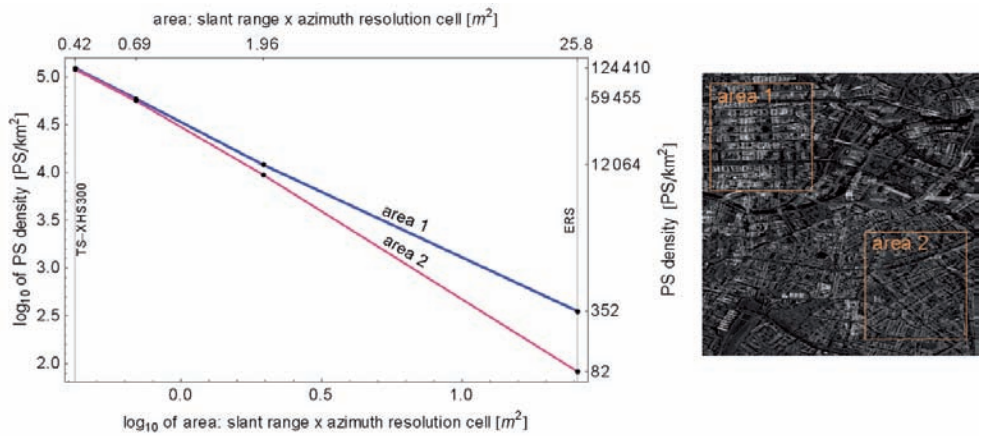

Fig. 8: PS density as a function of spatial resolution. The test site is the city of Berlin. Two areas with different urban development are selected. Area 1 has a high building density and area 2 is a typical urban area.

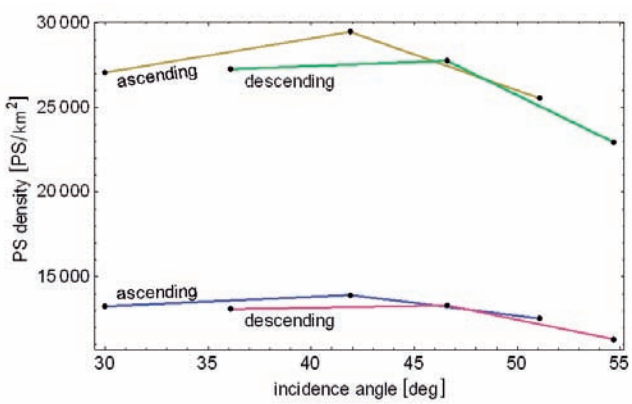

Fig. 9: PS density as a function of incidence angle. The PS density is measured in ascending and descending stacks and two different thresholds on the SCR for the PS detection are applied. The two upper graphs correspond to the low threshold resulting in a high PS density, while the lower ones show the distribution for the high threshold. Both thresholds are higher than the one used for Fig. 8. In princpile, flat look angles result in a loss of PS density because of shadowing. However, 42–47 deg look angle result in the highest PS density.

the subsidence of the building itself or of the pavement surrounding the building.

Many PS are structures acting as dihedral or trihedral reflectors. Assuming a background clutter of −4 dB and a PS detection threshold of 6 dB above clutter, then in ENVISAT/ASAR-type data an ideal full trihedral structure of about 30 cm side length is required to be detected as a PS. This estimation is based on the radar cross section (RCS) of a full trihedral $RCS = 12\,\pi\,a^4/\lambda^2$ a ground resolution of 24.4 m × 4.8 m. With TerraSAR-X high resolution spotlight mode and the same assumptions (i. e., a 23° look angle which results in a ground resolution of 1.5 m × 1.1 m) any full trihedral structure of 8 cm side length will be detected as a PS. These types of structures are typically plenty on modern building facades and can be well resolved due to the high resolution. Therefore, we can detect many PSs at a single building and are able to estimate deformation of the building itself. Our first experiences with TerraSAR-X high resolution spotlight date show typical PS densities of 124,000 PS/km^2, i. e., one PS per area of 2 m × 2 m. The PS density depends on resolution (cf. Fig. 8), incidence angle (cf. Fig. 9), and polarization. The increase of PSs with resolution is dramatic because the very high resolution fits well with the typical spatial scales of constructive elements at buildings. The loss of PS density at shallower incidence angles is due to partial shadowing of facades from adjacent buildings. The effect depends on the height of the building, its orientation, and its distance to other buildings.

5 SAR Tomography

Conventional SAR maps the 3D radar reflectivity distribution on ground into the 2D range-azimuth radar coordinate system. Consequences of this geometry are imaging ambiguities like layover, which are particularly pronounced in urban areas. SAR Tomography (TomoSAR) aims at accessing the third dimension, elevation (perpendicular to the range-azimuth plane), resolving layover, and mapping any scatterer in 3D coordinates (Reigber & Moreira 2000). TomoSAR uses stacks of several acquisistions from repeat orbits (and slightly different viewing angles) to establish a synthetic aperture in the elevation direction. In contrast to the – otherwise quite similar – synthetic aperture principle employed in the azimuth direction, TomoSAR must deal with sparse (typically only a few tens of acquisitions) and irregular sampling of the elevation aperture. The reflectivity distribution in the elevation direction for each range-azimuth pixel, and therefore the full 3D reflectivity distribution, is estimated by spectral analysis with special consideration of the mentioned difficulties caused by sparse and irregular sampling. The achievable resolution ρ_s in the elevation direction depends on the extent B_s of the elevation aperture, i. e., the maximum spatial baseline spread, via $\rho_s = \lambda r / 2B_s$ where λ is the wavelengh and r is range (in classical InSAR with baseline B_s, ρ_s is the elevation that causes an interferometric phase of 2π). Since the different acquisitions are taken at different times, possible motion of the sactterers has to be accounted for. Classical InSAR and PSI can be regarded as special cases of parametric TomoSAR.

From the reconstructed reflectivity profile in elevation, multiple layovered objects in any pixel are separated and the following information can be retrieved:

- *Number of scattering objects:* As essential prior knowledge for higher order PSI, the number of scatterers in a resolution cell can be estimated by applying model order selection schemes to the estimated reflectivity profile.
- *Reflectivity and elevation of the scattering objects:* It is obtained by implementing parameter estimation to the reflectivity profile estimates and leads to better localization and understanding of the scattering objects in three dimensions.

Like PSI, TomoSAR benefits greatly from the high resolution of TerraSAR-X data, as the density of coherent pixels and the signal-to-clutter ratio increase significantly with resolution.

In the following examples, TomoSAR is applied to TerraSAR-X high-resolution spotlight data acquired over the city of Las Vegas, USA. 16 scenes are used. The elevation resolution is about ρ_s = 40.5 m due to the limited baseline

range of the stack of 269.5 m. This, however, does not mean that individual scatterers can only be located to within this poor elevation resolution. The Cramér-Rao Lower Bound (CRLB) on elevation estimates can be shown to be:

$$\sigma_{\hat{s}} = \frac{\lambda r}{4\pi\sqrt{\mathrm{NOA}}\cdot\sqrt{2\,SNR}\cdot\sigma_{Bs}} \qquad (1)$$

where *NOA* is the number of acquisitions, SNR is the signal-to-noise ratio, and σ_{Bs} is the standard deviation of the baseline distribution. For instance, the stack used in this example has σ_{Bs} = 78.4 m, λ = 0.031 *m* and r = 704 km. Let us assume the SNR = 10 dB, the CRLB on elevation estimation is 1.24 m. With regular baseline distribution samples, the location accuracy can be related to the elevation resolution by:

$$\sigma_{\hat{s}} = \frac{0.39}{\sqrt{\mathrm{NOA}}\cdot\sqrt{SNR}}\,\rho_s\,. \qquad (2)$$

As input data to our tomographic algorithm we use TerraSAR-X data stacks generated by DLR's GENESIS PSI processor mentioned before. Fig. 10, left, shows the Wynn hotel in Las Vegas with a height close to 200 m, corresponding to an elevation range of 380 m. The middle image in Fig. 10 is the corresponding TerraSAR-X intensity image where green dots refer to selected PS points. The mean intensity image indicates that pixels containing multiple scatterers are mainly located at the intersection of the bright texture of the building with structures near ground. To exemplify the potential of the TomoSAR method, two pixels marked by red stars and a reference point marked by a yellow star have been selected and will be analyzed in the following. As P1 is located outside of the region of the high-rise building, it is expected that it only contains a single scatterer situated near the ground. By contrast, as P2 is located at the intersection area, we expect two scatterers inside this pixel, among them a weaker ground reflection and a stronger reflection from the building facade. The corresponding reflectivity estimates for those two pixels are shown in the right image of Fig. 10. Ground and building contributions can be well separated, even with such a small number of acquisitions. The spectral estimation method used for this elevation profiles was a singular value decomposition (SVD)-based approach (Fornaro et al. 2003) with singular value weighting according to the Wiener criterion (Zhu et al. 2009). In this example, we can see the potential of the tomographic approach to separate multiple scatterers in one cell using TerraSAR-X data.

With this convincing result of PS based tomography, a pixel based 3D focusing procedure is now applied to the same data stack. The Las Vegas convention center with a height of about 20 m as shown in the left image of Fig. 11 is a very interesting test building for 3D focusing as it is very large and has a regular shape. Therefore, we expect strong and stable returns which provide a very good starting point for

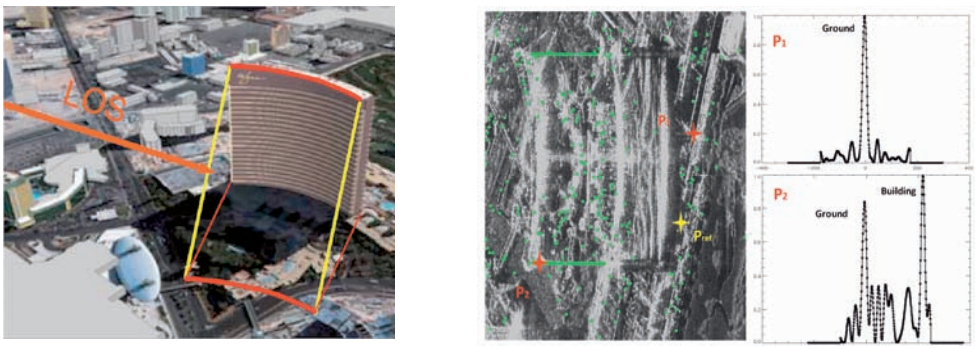

Fig. 10: Wynn Hotel, Las Vegas: Optical image (left) with viewing direction of SAR (LOS = line-of-sight) and two iso-elevation lines (yellow). Mean TerraSAR-X intensity image (center) with reference (yellow) and analysis points (red) P1 and P2. Reconstructed elevation profiles (right) for analysis points P1 (single scatterer) and P2 (two scatterers).

pixel-by-pixel 3D focusing. The right image of Fig. 11 shows the corresponding mean TerraSAR-X intensity image. Due to the limited extent of the investigated area phase errors caused by water vapor disturbances can be neglected. The reflectivity profile in elevation direction is reconstructed pixel by pixel. First the number of scatterers is estimated by model order selection based on the Akaike information criterion (SAKAMOTO et al. 1986), then reflectivity and elevation of each scatterer are estimated. Since the different acquisitions have been taken at different times, deformation must be considered, i. e., an additional velocity parameter is estimated in our SVD-Wiener algorithm, leading to a full 4D reconstruction. The left image of Fig. 12 shows the DEM generated from the elevation estimates (height relative to the reference point). The black cross marks the position of the selected reference point. Compared to the InSAR DEM generation procedure, TomoSAR overcomes layover and phase unwrapping problems. The full structure of the convention center has been captured at a very detailed level. For instance, different parts of the building have different heights, which is not visible in the Google Earth building model. Besides the building, more details such as the roads surrounding the convention center and even two bridges above the roads have been captured. There are still some distortions remaining in

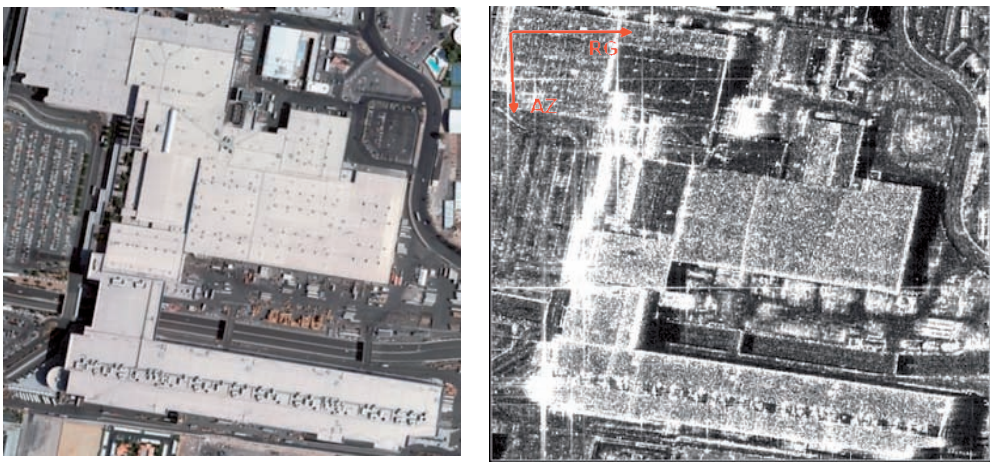

Fig. 11: Optical image of Las Vegas Convention Center (left) and corresponding mean TerraSAR-X intensity image (right).

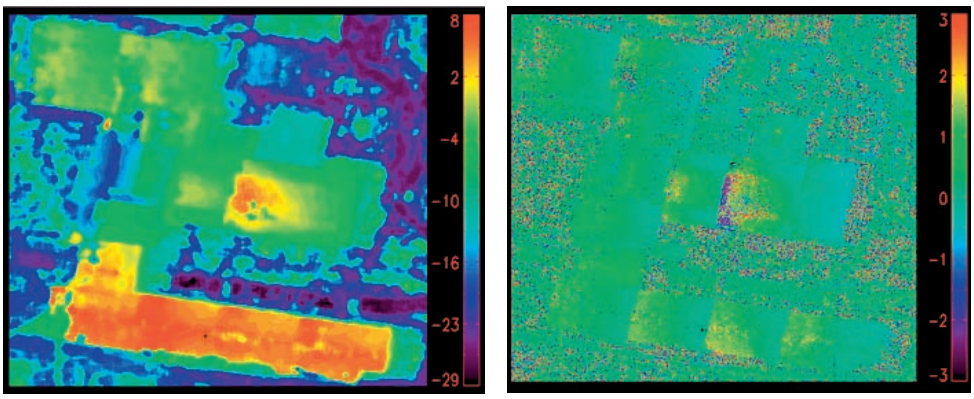

Fig. 12: Left: Generated DEM [unit: m]. Right: Extracted linear deformation velocity w.r.t. the reference point [unit: cm/y] (Black cross: reference point).

the middle of the image (red part) where a smooth roof is expected. It may be due to the incorrect linear deformation model assumption. The right image of Fig. 12 shows the extracted deformation velocity corresponding to the reference point. The deformation velocity map is consistent with the PSI processing result of Fig. 7. By checking the deformation of the distorted part mentioned above, unexpected significant subsidence appears which confirms again the incorrect linear deformation model assumption.

6 Feature and Speckle Tracking

The shrinkage or growth of glaciers and especially their flow velocity are indicators for subtle climatic changes. In the past InSAR techniques have proved to be useful tools for monitoring the remote ice sheets of Antarctica and Greenland (Gray et al. 1998; Joughin 2002), where conventional ground based measurements are not available. Today, high resolution systems such as TerraSAR-X have the potential to further improve the robustness of glacier velocity measurements and they even allow two derive accurate two dimensional motion fields.

SAR interferometry allows the measurement of glacier motion in the radar line of sight with sub-wavelength accuracy, i. e., millimeters to centimeters, depending on the radar wavelength. Typically, the interferometric phase difference between two images taken in two consecutive orbital repeat cycles is exploited, but in many practical cases this method is much too sensitive for typical glacier velocities between 0.1 and 5 meters per day. A further problem arises if spatial velocity gradients lead to more than one fringe per sample which can not be resolved anymore. Assuming an interferometric phase determination accuracy of $\lambda/10$, velocity sensitivities of 0.8 mm/day are achieved with ENVISAT or 1.4 mm/day for TerraSAR-X. Using multiple repeat cycles further increases the sensitivity. Furthermore the InSAR method requires the surface to stay coherent between the times of the repeated observations. This assumption usually holds if the time between acquisistions is short, like the one day during the ERS-1/ERS-2 tandem campaign 1996–2000, or the 3-day repeat orbital period during the ERS-1 ice orbit phase 1993/1994. However, it is seldom the case in the normal repeat cycles of SARs such as the 24-day repeat orbit of RADARSAT-1 and 2 or the 35 days of ERS

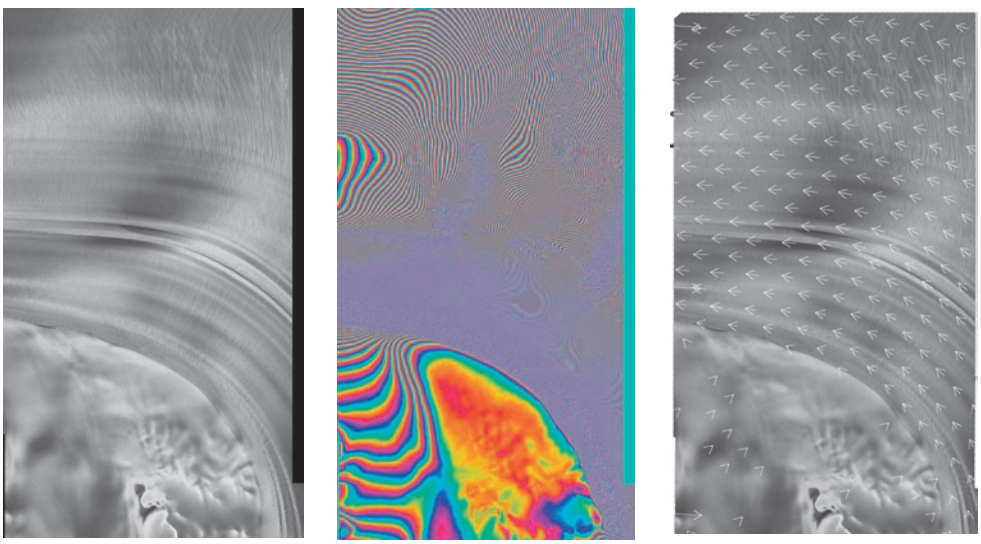

Fig. 13: Left: TerraSAR-X intensity image of the Antarctic Recovery glacier (30.10.2008). Center: 11 day interferogram (29 meter baseline). Right: Motion field derived from Speckle Tracking. Average coherence: 0.3. Horizontal direction (right): range. Vertical direction (up): azimuth.

and ENVISAT/ASAR. The TerraSAR-X orbital cycle of 11 days and the high resolution seem to be a good combination for coherent (speckle) and incoherent (feature) tracking.

Fig. 13 shows the TerraSAR-X intensity image of the Antarctic Recovery glacier and the interferogram generated from two images separated by 11 days. The great advantage of the method is evident: even in homogenous areas where the human eye can not identify any texture, the interferometric phase signal reveals surface motion. But a number of constranits impede the InSAR method: First, due to the 2pi-phase ambiguity in each SAR image only relative measurements are available between two points in the interferogram. Therefore, phase unwrapping and a reference point with known (e. g., zero) motion is required. Second, only the line-of-sight component of the surface motion is sensed by the radar, and the three-dimensional surface velocity vector must be derived by either using a DEM and downhill flow assumptions or, by combining satellite passes with different aspect angles. Third, InSAR suffers from decorrelation caused by all surface changes in the size of the wavelength. Such changes occur frequently on glaciers due to melting, rain, snowfall or structural deformation.

High resolution SAR sensors can overcome the above obstacles. Firstly, if image correlation techniques are applied (ignoring the interferometric phase information), ambiguity problems are obsolete. Both, coherent speckle (Gray et al. 2001) or incoherent features can be tracked with similar correlation methods. Especially coherent speckle tracking requires both images taken from the same position in space, i. e., from orbital repeat cycles. The major error sources for correlation techniques are: 1) atmospheric water vapor of max. 50 cm (range) depending on the humidity, 2) orbital errors on the order of 10 cm (range & azimuth), and 3) the accuracy of the correlation approach. The latter can be brought down to 10 centimeters and below by increasing the correlation chip size accordingly. The overall absolute accuracy of e. g., 50 cm/11 days = 4.5 cm/day is sufficient for many applications and can be increased easily by using local zero-motion-tie-points, increasing the correlation window or the time lag (increasing the time lag generally leads to decorrelation errors that overcompensates the gain in accuracy). Secondly, image correlation can be performed in both range and azimuth directions and therefore provides a two-dimensional motion vector. Thirdly, geometric phase decorrelation will impede the InSAR phase derivation but not image correlation as long as some object contrast is present, e. g., from crevasses or other surface structures.

Fig. 14 shows the correlation function between pairs of TerraSAR-X images with different coherence and surface characteristics. For convenience, TerraSAR-X EEC-SE products (Eineder 2005; Fritz & Eineder 2009) were used, i. e., spatially enhanced geocoded detected images with 1.25 m pixel spacing. In these products only about 1.3 looks are averaged to keep the highest quadratic spatial resolution. The small number of looks leaves a good part of the coherent speckle – wide band pseudo-noise that allows accurate correlation. Using these products all correlation can be easily performed in geocoded ground range pixels since co-registration and terrain compensation has been done in the TerraSAR-X SAR processor before.

The left image shows a patch of an Antarctic glacier (Recovery) with high coherence. In consequence the speckle signal delivers a well defined peak even on ice surfaces without object contrast. The correlation peak width is 4 pixels (6 meters). With the used correlation block size of about 2562 independent resolution cells (64 × 64 pixels) and the coherence of about 0.3 an accuracy of 0.029 pixels (0.037 meter) is estimated according to (Bamler & Eineder 2005).

The right image shows a patch of a glacier with significant surface changes within 11 days which lead to strong phase decorrelation. In consequence, coherent speckle tracking is no more possible and features have to be used to derive the motion field. The object contrast in Fig. 14 right is caused by crevasses. The achievable resolution now depends on the spatial structure of the features. High contrast and sharp features allow higher accuracy than slowly undulating patterns. In our experiments it turned out that about 4 × 4 = 16 looks may to be averaged to sufficiently reduce the amplitude of incoherent speckle maintaining

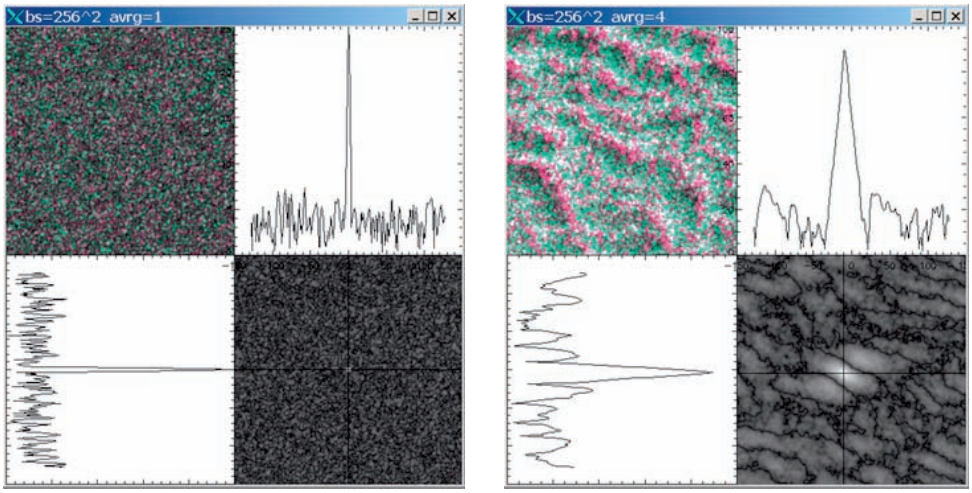

a) Recovery Ice Stream 11 days (coherent) b) Drygalski Glacier 11 days (incoherent)

Fig. 14: Correlation functions of TerraSAR-X images with 11 day interval. Upper left: multi-temporal color composite. Lower right: 2D-correlation function. Upper right: range cut through correlation maximum. Lower left: azimuth cut through maximum. a) Homeogeneous coherent glacier surface. Correlation peak width: 6 m. b) Decorrelated surface with crevasses. Resolution: 85 m and 72 m in range and azimuth, respectively. Window size: 256 × 256 pixels. Right image was averaged and decimated by a factor of 4 before correlation.

the signal of the lower resolution features. The width of the correlation peak is much wider than that of the speckle tracking result: 17 pixels in range and 12 in azimuth (85 m × 72 m). Correlation coefficient of the object features is much lower, in the order of 0.08. With the used correlation block size of 2562 resolution cells this transforms (Bamler & Eineder 2005) to an accuracy of 0.47 (East) and 0.33 (North) pixels corresponding to 2.3 m and 1.6 m.

In conclusion, relative accuracies of 0.3 cm/day and, depending on orbit errors and atmospheric conditions, absolute accuracies of 5 cm/day can be achieved by speckle correlation. 20 cm/day are achievable by feature correlation with rather simple methods. More details of the work performed by the authors can be found in (Rott et al. 2008) and (Floricioiu et al. 2008).

7 Outlook

Using different interferometric techniques a number of encouraging results were achieved within short time after the launch of TerraSAR-X. Some of them, such as glacier monitoring may be transferred to applications soon while more novel techniques such as TomoSAR will need more experiments to prove their applicability. In 2009 the launch of the co-operative sister satellite TanDEM-X will open even more opportunities for interferometric imaging by adding simultaneously acquired image pairs with high coherence.

Acknowledgements

The authors appreciate the contributions of Dana Floriciouiu for providing images from the TerraSAR-X Antarctic campaign.

References

Adam, N., Eineder, M., Schättler, B. & Yague-Martinez, N., 2007: First TerraSAR-X Interferometry Evaluation. – ESA FRINGE Workshop, Frascati.

Adam, N., Eineder, M., Yague-Martinez, N. & Bamler, R., 2008: High Resolution Interferometric Stacking with TerraSAR-X. – IEEE International Geoscience and Remote Sensing Symposium.

Adam, N., Parizzi, A., Eineder, M. & Crosetto, M., 2008: Practical Persistent Scatterer Processing Validation in the Course of the TERRAFIRMA Project. – Journal of Applied Geophysics, in print 2009.

Bamler, R. & Hartl, P., 1998: Synthetic Aperture Radar Interferometry. – Inverse Problems **14:** R1–R54.

Bamler, R. & Eineder, M., 2005: Accuracy of Differential Shift Estimation by Correlation and Split Bandwidth Interferometry for Wideband and Delta-k SAR Systems. – IEEE Geoscience and Remote Sensing Letters **2** (2): 151–155.

Buckreuss, S., Balzer, W., Mühlbauer, P., Werninghaus, R. & Pitz, W., 2003: The TerraSAR-X Satellite Project. – IEEE International Geoscience and Remote Sensing Symposium.

Eineder, M., Adam, N., Bamler, R., Yague-Martinez, N. & Breit, H., 2009: Spaceborne Spotlight SAR Interferometry with TerraSAR-X. – IEEE Transactions on Geoscience and Remote Sensing **47 (**5): 1524–1535.

Eineder, M., Schättler, B., Breit, H., Fritz, T. & Roth, A., 2005: TerraSAR-X SAR Products and Processing Algorithms. –IEEE International Geoscience and Remote Sensing Symposium.

Ferretti, A., Prati, C. & Rocca, F., 2001: Permanent Scatterers in SAR Interferometry. – IEEE Transactions on Geoscience and Remote Sensing **39 (**1): 8–20.

Ferretti, A., Savio, G., Barzaghi, R., Borghi, A., Musazzi, S., Novali, F., Prati, C. & Rocca, F., 2007: Submillimeter Accuracy of InSAR Time Series: Experimental Validation. – IEEE Transactions on Geoscience and Remote Sensing **45** (5): 1142–1153.

Floricioiu, D., Eineder, M., Rott, H. & Nagler, T., 2008: Velocities of Major Outlet Glaciers of the Patagonia Icefield Observed by TerraSAR-X. – IEEE International Geoscience and Remote Sensing Symposium.

Fornaro, G., Serafino, F. & Soldovieri, F., 2003: Three-dimensional focusing with multipass SAR data. – IEEE Transactions on Geoscience and Remote Sensing **41** (3): 507–517.

Fritz, T. & Eineder, M., 2009: TerraSAR-X Ground Segment – Basic Product Specification Document. – TX-GS-DD-3302, Revision 1.6, available online.

Gray, A.L., Mattar, K.E. & Vachon, P.W., 1998: InSAR results from the RADARSAT Antarctic Mapping Mission Data: Estimation of Glacier Motion using a Simple Registration Procedure. – IEEE International Geoscience and Remote Sensing Symposium: 1638–1640.

Gray, A.L., Short, N., Mattar, K.E. & Jezek, K.C., 2001: Velocities and flux of the Filchner ice shelf and its tributaries determined from speckle tracking interferometry. – Canadian Journal of Remote Sensing **27** (3): 193–206.

Joughin, I., 2002: Ice-sheet velocity mapping: a combined interferometric and speckle-tracking approach. – Annals of Glaciology **34**.

Reigber, A. & Moreira, A., 2000: First demonstration of airborne SAR tomography using multibaseline L-band data. – IEEE Transactions on Geoscience and Remote Sensing **38** (5): 2142–2152.

Rott, H., Eineder, M., Nagler, T. & Floricioiu, D., 2008: New results on dynamic instability of Antarctic Peninsula glaciers detected by TerraSAR-X ice motion analysis. – European Conference on Synthetic Aperture Radar (EUSAR).

Sakamoto, Y., Ishiguro, M. & Kitagawa, G., 1986: Akaike information criterion statistics. – Reidel, Dordrecht, The Netherlands.

Zhu, X., Adam, N., Brcic, R. & Bamler, R., 2009: Space-borne High Resolution SAR Tomography: Experiments in Urban Environment Using TerraSAR-X Data. – Joint Urban Remote Sensing Event 2009, Shanghai, China.

Addresses of the Authors:

Prof. Dr.-Ing. habil. Richard Bamler, Dr. rer. nat. Michael Eineder, Nico Adam, Remote Sensing Technology Institute (IMF), German Aerospace Center (DLR), Oberpfaffenhofen, 82234 Wessling, Germany, Tel.: +49-8153-28-2673, -1396, -1326, Fax: -1420, e-mail: richard.bamler@dlr.de, michael.einder@dlr.de, nico.adam@dlr.de

Prof. Dr.-Ing. habil. Richard Bamler, Xiaoxiang Zhu, Stefan Gernhardt, Technische Universität München, Lehrstuhl für Methodik der Fernerkundung, Institut für Photogrammetrie und Kartographie, Arcisstraße 21, 80333 München, Germany, Tel.: +49-8153-28-2673, Fax: -1420, e-mail: richard.bamler@dlr.de, xiaoxiang.zhu@bv.tum.de, Stefan.Gernhardt@bv.tum.de.

Manuskript eingereicht: Mai 2009
Angenommen: Juli 2009